Southern Ocean Phytoplankton Blooms Observed by Biogeochemical Floats

Takaya Uchida[1*], Dhruv Balwada[3], Ryan Abernathey[1,2], Channing Prend[4], Emmanuel Boss[5], and Sarah T. Gille[4]

[1]Department of Earth and Environmental Sciences, Columbia University in the City of New York
[2]Division of Ocean and Climate Physics, Lamont-Doherty Earth Observatory
[3]Center for Atmosphere Ocean Science, Courant Institute of Mathematical Sciences, New York University
[4]Scripps Institution of Oceanography, University of California, San Diego
[5]School of Marine Sciences, University of Maine

Key Points:

- In-situ estimates of phytoplankton biomass and its seasonal cycle are derived based on optical backscatter from biogeochemical Argo floats.
- Depth integrated biomass peaks after mixed layers start shoaling, but accumulation rates turn positive when mixed layers are deepening.
- Biomass is low in Ekman downwelling regions and high in the Antarctic Circumpolar Current and seasonal sea-ice zone.

*205A Oceanography, Lamont-Doherty Earth Observatory, New York

Corresponding author: Takaya Uchida, takaya@ldeo.columbia.edu

Abstract

The spring bloom in the Southern Ocean is the rapid-growth phase of the seasonal cycle in phytoplankton. Many previous studies have characterized the spring bloom using chlorophyll estimates from satellite ocean color observations. Assumptions regarding the chlorophyll-to-carbon ratio within phytoplankton and vertical structure of biogeochemical variables lead to uncertainty in satellite-based estimates of phytoplankton carbon biomass. Here, we revisit the characterizations of the bloom using optical backscatter from biogeochemical floats deployed by the Southern Ocean Carbon and Climate Observations and Modelling (SOCCOM) and Southern Ocean and Climate Field Studies with Innovative Tools (SOCLIM) projects. In particular, by providing a three-dimensional view of the seasonal cycle, we are able to identify basin-wide bloom characteristics corresponding to physical features; biomass is low in Ekman downwelling regions north of the Antarctic Circumpolar Current (ACC) region, and high within and south of the ACC.

Plain language summary

The advent of satellites has allowed us to observe the ocean surface at unprecedented scale. One of the major biogeochemical findings from these observations were that phytoplankton in the Southern Ocean repeatedly go through a dramatic phase of growth every spring. Phytoplankton, however, do not only exist at the ocean surface but in the interior as well, generally in the top 100 m. In our study, we revisit the characterization of this spring growth using autonomous floats that vertically profile biogeochemical properties including phytoplankton concentration. Using three-dimensional estimates of phytoplankton, our results support the conventional knowledge of there being a robust seasonal cycle in phytoplankton.

1 Introduction

Phytoplankton are the primary photosynthesizers that convert energy from the sun to a form that is available to sustain marine life and are critical to the biological carbon pump (Deppeler & Davidson, 2017). The biological carbon pump, which involves the production of organic carbon via photosynthesis and export to depth, is argued to be responsible for maintaining $\sim 90\%$ of the vertical dissolved inorganic carbon (DIC) gradient (Sarmiento, 2013) and $\sim 10\%$ of the total carbon flux to the deep ocean (Siegenthaler & Sarmiento, 1993). While there is no evidence for any recent global-scale changes in

the biological carbon pump (McKinley et al., 2017), its contribution to carbon sequestration may decline in a future warming climate (J. Moore et al., 2013; Osman et al., 2019). Consequently, phytoplankton and biological activity are important contributors to both natural and anthropogenic carbon sequestration via export production and maintaining the DIC gradient (Gruber et al., 2019).

The Southern Ocean, along with the overturning circulation (Marshall & Speer, 2012), plays a central role in global biological production. Macro-nutrients such as phosphate and nitrate are upwelled in the Southern Ocean along with circumpolar deep water, but these nutrients are not fully consumed due to iron limitation (Field et al., 1998; C. Moore et al., 2013; Williams & Follows, 2011). The underutilized macro-nutrients are circulated to the rest of the ocean basins where they replenish the nutrient depleted surface waters (Parekh et al., 2004; Dutkiewicz et al., 2005; J. Moore et al., 2013). While the outcropping of isopycnals in the Southern Ocean make it a globally important region for physical carbon exchange with the deep ocean (Lévy et al., 2013), the importance of Southern Ocean carbon export via sinking and subduction of organic carbon is less certain–estimates range from 8-40% of the global export production (Schlitzer, 2002; Siegel et al., 2014; Stukel & Ducklow, 2017). Therefore, a better understanding of the annual cycles of Southern Ocean phytoplankton, which are at the base of marine food webs, can help in better constraining global biological production and local export production.

Estimates of remotely sensed chlorophyll concentration have been one of the primary ways to glean insight into the basin-wide magnitude and temporal variability of these blooms (e.g. J. Moore & Abbott, 2000; Thomalla et al., 2011; Sallée et al., 2015; Ardyna et al., 2017). These studies have shown that the peak of surface chlorophyll concentrations observed under clear-sky conditions in the Antarctic Circumpolar Current (ACC) region tends to be during December and January, coinciding with the periods when the surface ocean is warming and mixed layers are shoaling. Primary production estimates based on these satellite observations of chlorophyll and/or optical backscatter, and estimates of photosynthetically active radiation (PAR) and temperature, range from 10-200 g C m^{-2} yr^{-1} in the open Southern Ocean (Arrigo et al., 2008; Westberry et al., 2008; Silsbe et al., 2016). While these studies have greatly enhanced our understanding of Southern Ocean biomass, they are limited as satellites only observe the surface concentrations. Behrenfeld (2010) has shown that only knowing the surface concentrations is not suf-

ficient to understand phytoplankton bloom phenology, as periods with deep mixed layers can have active growth that is not easily captured in the surface concentration signal. To circumvent this issue, some recent studies have calculated phytoplankton biomass in the surface ocean by assuming that phytoplankton are vertically homogeneous in the mixed layer (e.g. Sallée et al., 2015). Carranza et al. (2018) recently showed, however, that the biogeochemistry can restratify fairly quickly on the order of 3-5 days, resulting in vertical gradients of phytoplankton within the mixed layer.

In this study, we assess the seasonal cycle of phytoplankton variability in the Southern Ocean by taking advantage of the new biogeochemical (BGC) Argo floats deployed by the Southern Ocean Carbon and Climate Observations and Modeling (SOCCOM) and Southern Ocean and Climate Field Studies with Innovative Tools (SOCLIM) projects. The main focus of our work is to revisit the characterization of the annual cycles of phytoplankton blooms, and to understand the dynamics of these cycles. While this is the first study to use in-situ BGC Argo floats to characterize bloom phenologies in the Southern Ocean, BGC Argo floats have already started to provide a wealth of insight into the biogeochemistry at work in the Southern Ocean (e.g. Bushinsky et al., 2017; Briggs et al., 2018; Gray et al., 2018; Carranza et al., 2018). Johnson et al. (2017) reported the annual net community production (ANCP), which approximately balances the annual carbon export production, using the nitrate sensors from the floats. Their study is complementary to our work, as they report on the export of total organic carbon from the surface to interior, while we report on the growth and decay of the phytoplankton themselves. BGC Argo floats and gliders equipped with similar sensors have also been used to investigate bloom dynamics in the North Atlantic (Boss & Behrenfeld, 2010; Erickson & Thompson, 2018; Mignot et al., 2016, 2018) and Southern Ocean (Swart et al., 2015).

The main results of this study are zonally averaged monthly climatologies of phytoplankton biomass and accumulation rates for the Atlantic, Indian and Pacific Ocean sectors of the Southern Ocean. These climatologies show that, while the biomass peaks in spring/summer, accumulation generally starts significantly earlier – during the phase when mixed layers are still deepening. We also present the variability of bloom timings and growth rates in different regions and put the results in the context of theoretical ideas about phytoplankton blooms in the Southern Ocean.

2 Theory of Phytoplankton Dynamics

Phytoplankton biomass is usually modeled as a concentration field that evolves according to the advection-diffusion equation, along with sources and sinks driven by cell division and loss by mortality and grazing respectively. This is written as,

$$\frac{\partial P}{\partial t} + \nabla \cdot (\mathbf{v}P) = (\mu - l)P + \nabla \cdot \kappa \nabla P + w_{\mathrm{s}} \frac{\partial P}{\partial z}, \tag{2.0.1}$$

where $\mathbf{v}$ is the 3D non-divergent velocity field; $\nabla\cdot$ the 3D divergence; κ the small-scale turbulent diffusivity; w_{s} the sinking velocity; $\mu(x, y, z, t)$ the phytoplankton division rate, which is a balance between photosynthesis and respiration, and generally depends on nutrient availability, light and temperature and $l(x, y, z, t)$ the loss rate due to biological processes: mortality and grazing.

It is common to average this equation appropriately and impose assumptions, such that the averaged equation describe the evolution of bulk phytoplankton biomass on seasonal time scales (e.g. Behrenfeld, 2010; Mignot et al., 2016, 2018). The horizontal averaging is formally done spatially over length scales of a few eddies and temporally over a few eddy turnover times (∼seasonal time scales), and it is assumed that horizontal flux divergence on the left hand side is small. This results in a 1-dimensional model for evolution of phytoplankton concentrations. This assumption is a pragmatic one, and partially supported by the observation that the seasonally evolving biogeochemical patterns show spatial coherence over large areas (J. Moore & Abbott, 2000; Mazloff et al., 2018). It is also common to consider the evolution of vertically integrated biomass, rather than trying to describe the evolution of the vertical profile. Conventionally, this vertical integration is considered over a region where phytoplankton can reproduce, and referred to as the productive layer. Note that the productive layer can be deeper than the euphotic layer due to vertical migration of phytoplankton (Forward, 1976) or if mixing is vigorous enough to ensure that phytoplankton spend sufficient time in the euphotic layer to grow. We show our definition of the productive layer in Section 3. The horizontally averaged and vertically integrated bulk phytoplankton biomass equation is,

$$\left\langle \frac{\partial P}{\partial t} \right\rangle = \langle \mu P \rangle - \langle l P \rangle + w^*(-H)P(-H) - \kappa_v \frac{\partial P}{\partial z}\Big|_{z=-H}, \tag{2.0.2}$$

where the brackets indicate vertical integral over the depth of the productive layer ($\langle\cdot\rangle = \int_{-H}^{0}(\cdot)\, dz$). Note that the variables now represent horizontal and temporally averaged/smoothed variables. Here, w^* is composed of time and space averaged vertical velocities, eddy driven

mean vertical velocities (Gent et al., 1995; Fox-Kemper et al., 2008), and sinking of phytoplankton (Williams & Follows, 2011). The vertical diffusivity (κ_v) is a result of turbulence driven by winds, shear, and buoyancy driven convection that is active in maintaining the mixed layer, and also the vertical projection of along isopycnal stirring by submesoscale and mesoscale eddies (Redi, 1982; Balwada et al., 2018). The last two terms in equation 2.0.2 are evaluated at the base of the productive layer ($-H$), and act as sinks on the bulk biomass because there are no signficant phytoplankton concentrations below the productive layer.

The vertically integral of biomass change on the left-hand side of eqn. 2.0.2 can be formally expanded and normalized as, $\frac{1}{\langle P \rangle} \left\langle \frac{\partial P}{\partial t} \right\rangle = \frac{1}{\langle P \rangle} \left[\frac{\partial \langle P \rangle}{\partial t} - P(-H) \frac{\partial H}{\partial t} \right]$, where H is the depth of the productive layer, and not the mixed layer as commonly considered. The first term on the right-hand side represents the change in bulk biomass, and the second term becomes negligible at the base of productive layer, i.e. $P(-H) \approx 0$. The above discussion leaves us with an equation for the accumulation rate,

$$r_{\mathrm{p}} \approx \frac{1}{\langle P \rangle} \frac{\partial \langle P \rangle}{\partial t} = \mu_{\mathrm{p}} - l_{\mathrm{p}}, \tag{2.0.3}$$

as a balance between bulk primary production ($\mu_{\mathrm{p}} = \langle \mu P \rangle / \langle P \rangle$) and bulk losses ($l_{\mathrm{p}} = (\langle lP \rangle + \kappa_v \frac{\partial P}{\partial z}\big|_{z=-H}) / \langle P \rangle$) (Behrenfeld & Boss, 2018). In this study we will estimate the bulk biomass ($\langle P \rangle$) and accumulation rate (r_{p}) using observations, and the above presentation will help us identify potential mechanisms that may be driving and setting the observed patterns for these variables.

3 Data and Methods

In this study we use profiling Argo floats that were deployed as part of the Southern Ocean Carbon and Climate Observations and Modeling (SOCCOM), and Southern Ocean and Climate Field Studies with Innovative Tools (SOCLIM) projects. The SOCCOM floats were APEX and BGC-Navis (Johnson et al., 2017; Riser et al., 2018), while the SOCLIM floats were PROVBIO-2 and PROVAL (Leymarie et al., 2018). All floats were equipped with CTD and bio-optical sensors, which measured temperature, salinity, pressure, nitrate, dissolved oxygen, chlorophyll fluorescence and optical backscatter coefficient. Additionally, the SOCLIM floats measured incoming PAR. Figure 1 shows a summary of the raw data used in this study, which are composed of 152 (144 SOCCOM, 8 SOCLIM) BGC Argo floats. Data from April 2014 to May 2019 were used, but a sig-

nificant boost in sampling happened in 2016 (Fig. 1**a**). Most of the sampling is around the ACC region, with less sampling in the gyres to the north and Weddell Sea to the south. There is also minor zonal asymmetry in sampling, with less sampling in the Atlantic sector relative to the Indian and Pacific sectors.

We only used the quality controlled data here; this included data points that had been flagged as good or had been corrected by inspection (as indicated by quality flags– 1, 2, 5 and 8 (Carval et al., 2014, `https://archimer.ifremer.fr/doc/00187/29825/40575.pdf`)). In-situ temperature and salinity measurements were used to calculate the potential density and stratification (N^2) using the Python implementation of the Thermodynamic Equation of Seawater 2010 (TEOS-10; McDougall & Barker, 2011, `https://teos-10.github.io/GSW-Python/`). The mixed-layer depth was defined using the density threshold criteron: the depth at which the density is greater by 0.03 kg m^{-3} relative to 10 dbar (de Boyer Montégut et al., 2004; Carranza et al., 2018; Ardyna et al., 2019). Figures S4-S6 shows that this criterion picks up the sharp vertical gradient in stratification.

For the biogeochemical properties of chlorophyll and backscatter, additional processing was required. We used the chlorophyll concentrations that have been corrected for nonphotochemical quenching and the optical backscatter measured at 700 nm. We subtracted out the median of all measurements per float below 600 dbar, and then applied a five-point median filter in the vertical to remove the spikes in the profile. Similar methods have been used previously (e.g. Carranza et al., 2018; Mignot et al., 2018; Erickson & Thompson, 2018). The removal of the deep median assumes that non-zero values at depth are generally a result of an instrument bias rather than true phytoplankton related signal. The despiking removes measurement noise or potential signal due to aggregates. In order to correct for the known bias between measurements by Argo floats and shiptrack high-performance liquid chromatography (HPLC), we first doubled the corrected chlorophyll concentrations to account for the global factor of 2 (Roesler et al., 2017) and then adjusted them based on an empirical fit for each dataset: $\mathrm{Chl}_{\mathrm{HPLC}} \approx 0.21\times \mathrm{Chl}^{0.714}_{\mathrm{SOCCOM}}$ (Johnson et al., 2017; Haëntjens et al., 2017) and $\mathrm{Chl}_{\mathrm{HPLC}} \approx \mathrm{Chl}_{\mathrm{SOCLIM}}/3.46$ (Roesler et al., 2017, Table 1 in their paper). Henceforth, we drop the subscript $(\cdot)_{\mathrm{HPLC}}$, i.e. $\mathrm{Chl} = \mathrm{Chl}_{\mathrm{HPLC}}$.

Phytoplankton carbon biomass was estimated using the backscatter data. This process required first converting the backscatter observations at 700 nm to 470 nm, using $b_{bp}(470) = b_{bp}(700)\left(\frac{470}{700}\right)^{-0.78}$. Then the estimated 470 nm backscatter was converted to phytoplankton carbon biomass (C_p) using the empirical linear relationship from Graff et al. (2015).: $C_p = 12128\ b_{bp}+0.59$. This relationship was obtained by comparing simultaneous measurements of in-situ phytoplankton carbon biomass and backscatter, using data from cruises in the North and South Atlantic, and the Western Pacific Ocean. The R^2 coefficient of the linear regression was 0.69, and the root-mean-square error in phytoplankton carbon biomass around the empirical relationship 4.6 mg C m^{-3}. While this empirical relationship is not perfect, it has previously been applied to estimate net primary production (NPP) globally (Silsbe et al., 2016), C_p in the Southern Ocean (Haëntjens et al., 2017), and is consistent with Behrenfeld et al. (2005) in which NPP was first derived based on b_{bp}.

As different floats had different temporal and vertical sampling frequencies, we interpolated the data for each float onto uniform temporal grids with time steps equal to the minimum temporal sampling rate for each float, and a stretched pressure grid between 4-1000 dbar with resolution of 4 dbar near the surface and 10 dbar toward the bottom. The interpolation was done in Python using a piecewise cubic hermite interpolating polynomial (pchip) scheme. In order to avoid including non-phytoplankton particulate organic matter in our calculation, we masked the backscatter data using a mask that was built under the assumption that phytoplankton biomass would have appreciable levels of associated chlorophyll. A cut-off Chl per float was defined as the 90^{th} percentile of concentrations deeper than 200 dbar, viz., we mask out C_p and Chl below this concentration. The bulk biomass $\langle C_p \rangle$ is then defined by vertically integrating the masked C_p over the whole water column. The depth of 200 dbar was chosen as it was always deeper than the depth where PAR attenuated to one percent of its surface value (h_{PAR}; Fig. S1). Here h_{PAR} was estimated from the empirical relation provided by Morel et al. (2007, eqn. 10 in their paper, using surface Chl as the average of top 50 dbar similar to what satellites would observe.). The bulk biomass $\langle C_p \rangle$ was insensitive to this depth scale (200 dbar) and percentile value (90%) chosen for masking out backscatter below the productive layer; our algorithm was able to capture phytoplankton within the mixed layer year round, and the difference in the parameter choice only affected the depth below the mixed layer at

which backscatter was masked out (Figs. 2, S4-S6). We show the robustness of our algorithm in Fig. S2 by changing these parameters.

The floats are advected approximately with the flow at 1000 m. Thus, changes in the time series of phytoplankton observed by an individual float can potentially be a result of a float crossing through a region of distinct productivity, or a patch of distinct productivity at the surface being advected relative to the flow at 1000 m. However, averaging over large regions and performing a temporal smoothing to extract only the slowly varying seasonal signal, as done in Section 4, allows us to capture the broad regional-scale seasonal signals of phytoplankton evolution, which are of interest in this work. This notion is supported by previous studies that observed broad regions over which similar seasonal cycles manifest themselves (Thomalla et al., 2011; Ardyna et al., 2017). Additionally, apart from the floats in the ACC, most floats do not traverse very large distances over a year, and so the results are not expected to be contaminated by a single float having seen two dramatically different phytoplankton blooms in a year of sampling. The precise impact and the biases introduced by the float sampling with a coarse temporal resolution ($\sim$10 days) on quantifying synoptic evolution, which is not the focus here, could be addressed in the future using an Observing System Simulation Experiment (OSSE).

While considering potential mechanisms that describe the observed patterns, we employ the surface heat flux and surface wind stress from the Biological Southern Ocean State Estimate reanalysis (BSOSE; Verdy & Mazloff, 2017), and AVISO based surface geostrophic eddy kinetic energy (EKE; `https://www.aviso.altimetry.fr`).

4 Results

4.1 Biomass Cycles from Individual Floats

The Southern Ocean is known to have a wide variety of distinct cycles of biomass growth and decay, as observed by satellites (Sallée et al., 2015; Ardyna et al., 2017). These cycles are generally associated with light availability, circulation, mixed-layer properties and external iron sources in the region. Here we show three qualitatively different cycles observed by three individual SOCCOM floats, with insight from previous studies that the seasonal sea ice zone (SIZ), Antarctic Circumpolar Current (ACC), and subtropical zone (STZ) have distinct bloom phenologies (Arrigo et al., 2008; Sallée et al., 2015). The mean locations of these floats are indicated in Fig. 1**b**. We will use the terminol-

ogy *onset*, *climax* and *apex* to characterize the bloom cycle (Behrenfeld, 2010). Each phase is defined using the time series of the vertically integrated biomass ($\langle C_p \rangle$) as i) *onset*: $\langle C_p \rangle$ minimum and $r_p = 0$, ii) *climax*: r_p maximum, and iii) *apex*: $\langle C_p \rangle$ maximum and $r_p = 0$, where r_p was calculated from eqn. 2.0.3 by substituting P with C_p (Llort et al., 2015; Sallée et al., 2015; Behrenfeld & Boss, 2018; Mignot et al., 2018). The vertically integrated biomass time series discussed in this study, examples shown in Fig. 2**d**-**f**, have been smoothed using a 30-day running mean. This smoothing extracts the seasonal cycle and removes synoptic signals, which are not well resolved due to the 10-day sampling frequency of most SOCCOM floats. As the time series presented here might potentially be sensitive to the possibility of floats traversing from one biogeochemical region to another, we purposely chose floats that stayed more or less in the same biogeochemical region (Ardyna et al., 2017) and did not show dramatic changes in water mass properties.

The first float (float ID: 5904184) is located south of the climatological Polar Front (PF) in the Ross Sea, which is a region covered by sea ice with limited PAR during austral winter (Fig. 2**a**). This particular float happened to be under ice from around July to November, as indicated by the missing data in the top 10 dbar for this period when the float's ice detection algorithm did not allow it to surface. During the period of ice coverage, both the phytoplankton biomass concentration C_p and bulk phytoplankton biomass $\langle C_p \rangle$ were negligibly small. The melting of sea ice at the end of November, which allows light to enter the water column and presumably also supplies iron, is coincident with a massive growth in phytoplankton with $r_p \approx 0.07$ day^{-1} at its climax (Fig. 2**d**). This also happens at the time when the mixed layer is at its shallowest, and phytoplankton spend all their time in the euphotic layer. Surface biomass concentration C_p^{surf} is consequently tightly coupled with $\langle C_p \rangle$ throughout the bloom cycle. However, this growth is short lived, approximately 1-2 months, and the bloom starts to decay by the end of January.

The second float (float ID: 5904683) is located downstream of the Kerguelan Plateau and drifts along the Antarctic Circumpolar Current (ACC; Fig. 2**b**). This is a region of vigorous eddy activity, and the presence of the Kerguelan Islands and hydrothermal vents can act as a source of lithogenic/benthic iron here (Gille et al., 2014; Swart et al., 2015; Ardyna et al., 2019). This float happened to see a short-lived period of growth in July, but the onset to apex is from August till the end of December. Considering that the on-

set is before the wintertime mixed-layer depth maximum, it is likely that increase in phytoplankton is due to the reduction of grazing pressure (Behrenfeld, 2010). The climax ($r_{\mathrm{p}} \approx 0.02$ day^{-1}) is during a period when the mixed layer is deepening, while the maximum in surface concentrations and bulk biomass are seen when the mixed layers are their shallowest (Fig. 2**e**). During the period when the mixed layers are shallow, between December and February, instances of phytoplankton biomass existing below the mixed layer depth are also observed.

The last float (float ID: 5904395) considered in this section is located in the quiescent Pacific STZ (Fig. 2**c**). This is a region where light is plentiful year round, but macronutrients might be limited due to the presence of a strong thermocline (Carranza & Gille, 2015). The deepest observed mixed layers (~ 100 m) are not significantly different from the expected depth of the euphotic layers. This float experiences slow biomass accumulation ($r_{\mathrm{p}} < 0.01$ day^{-1}) onsetting in July and extending all the way till February, along with short periods of decay during this period during November and January (Fig. 2**f**). This bloom cycle is quite different from the two discussed above, as there is no single dominant apex but instead a broad period when bulk biomass fluctuates at values slightly greater than the annual background with the majority of phytoplankton existing below the mixed layer during austral summer (October-February). Carranza and Gille (2015) found evidence that transient mixed layer deepening associated with high frequency winds can supply nutrients that alleviate the nutrient limitation both in the ACC and subtropical latitudes, driving episodic increases in productivity with stronger signals in the latter zone.

It should be noted that only the under-ice float observes periods where the bulk biomass becomes negligibly small during onset, while the other two floats observe regions where there is a non-negligible level of background bulk biomass year round using backscatter as a proxy. It is possible that non-phytoplankton sources can produce non-zero backscatter signal during parts of the year, but our algorithm to account for backscatter only coinciding with chlorophyll reduces this possibility. We believe that, while using backscatter as a proxy may not be an exact estimator of phytoplankton concentrations and bulk phytoplankton biomass estimates, it presents a faithful pattern of observed temporal variability, which is the focus of this study.

4.2 Temporal and Spatial Variability in Bloom Phenology

In the above section we showed that the bloom cycles can be described by the timing of the three phases: onset, climax and apex. While synoptic variability can complicate the precise timing of each phase, they are useful to qualitatively distinguish blooms. Here, we present the median and distribution of the different bloom phase timings and strength of the bloom itself to draw basin-wide characterizations. While it is common to separate biogeochemical zones based on the ACC frontal positions (Sallée et al., 2015; Gray et al., 2018), here we simply chose zones based on latitudinal bands: north of 45S (n45), between 45-60S, and south of 60S (s60). This is appropriate for our purposes because we consider the three sectors of the Southern Ocean: Atlantic (70E-20W), Indian (20W-180W), and Pacific (180E-70E) separately, and the mean frontal locations in each individual sector are quasi-zonal. In order to avoid detecting erroneous minima and maxima in $\langle C_p \rangle$ and r_p due to some time series starting or ending mid year, we require each yearly time series to start before July and end after October when detecting the *onset*, start before August and end after November for *climax*, and start before October and end after December for *apex*. The five-year long data set, starting on April 7, 2014 and ending on May 11, 2019, yielded a total of 228 onset, 222 climax and 229 apex events (Fig. S13).

Figure 3 shows the box plots of the timing of each bloom phase and deepest mixed layer for different latitudinal bands and sectors. The median onset timing shifts from around June-July in the northern most latitudinal range (n45) to August-September in the southern most latitudinal range (s60). Correspondingly the median apex timing shifts from October-December in n45 to January-February in s60, with the climax lying in the middle. The large range (3-6 months), in the timing of the different phases is a probably a combined result of spatial and internannual variability. The range of the onset timing is generally a bit smaller than the range of climax or apex timing, suggesting that blooms have a relatively well defined onset timing. The shift in onset time to later in the year further south, and its narrow range, confirms that the well-defined annual cycle of insolation, influencing both light availability and mixed-layer depth, is the primary control on initiating the bloom.

The timing of mixed-layer depth maxima relative to the onset date shows that in the latitude bands north of 60S, the bloom begins while the mixed layer is still deepen-

ing, while the climax happens after the mixed layer has started to shoal; bloom onset occurs in winter/autumn and blooms ramp up in production in the spring. The blooms to the south of 60S, however, most of which are in SIZ, have a different phenology. Here bloom onset occurs generally after the timing of the deepest mixed layers, when the mixed layers have started to shoal. This is likely because the melting of the sea ice releases iron (Boyd & Ellwood, 2010), allows PAR to penetrate into the surface waters, and causes the mixed layer to shoal, all factors that help phytoplankton grow. Prior to the receding of sea ice, the SIZ also experiences polar night and is severely light limited. The time lag between each phase in s60 is also shorter relative to the northern regions, presumably due to the growth season being shorter.

We now move onto the spatial variability in bloom phenology that is observed in the accumulation rates and strength of the spring blooms. We define two metrics: the rate of increase in biomass at i) the bloom climax ($r_{\mathrm{p}}^{\mathrm{climax}}$) and ii) between the onset and apex, i.e. r_{ao} ($= \frac{\Delta \ln [\langle \mathrm{C_P} \rangle]}{\Delta t}$) where the difference is taken between the two phases. The former indicates the rate at which biomass increases most rapidly per bloom, and the latter is the normalized amplitude of the entire bloom cycle, i.e. the bloom strength. The two rates ($r_{\mathrm{p}}^{\mathrm{climax}}$ and r_{ao}) are plotted against geographical locations in Fig. 4; $r_{\mathrm{p}}^{\mathrm{climax}}$ is larger than r_{ao}, as expected because the latter assumes an exponential growth over the entire bloom cycle. Both rates have higher magnitudes in the south compared to the north, particularly to the south PF in the SIZ (Fig. 4). There is also some suggestion of elevated production in regions where the ACC interacts with topography, such as the Drake Passage, the Kerguelen Plateau, and the Pacific Antarctic ridge, consistent with the findings by Ardyna et al. (2019); Prend et al. (submitted). Better data coverage would be required, however, to confirm the zonal variations in accumulation rates that might be present in each sector.

We also plot the mean rates of Ekman pumping calculated from BSOSE outputs of wind stress ($w_{\mathrm{E}} = \frac{1}{\rho_0 f} \hat{\mathbf{z}} \cdot \nabla \times \tau$), and eddy kinetic energy (EKE) observed from AVISO SSH fields in Fig. 4. The Ekman pumping shows the widely known pattern of downwelling ($w_{\mathrm{E}} < 0$; blue) in the subtropical gyres to the north of the ACC and upwelling ($w_{\mathrm{E}} > 0$; red) in the ACC and south of it. The EKE is highest in the ACC, particularly over regions where the ACC interacts with topography (Wilkin & Morrow, 1994). There is an apparent correspondence between $r_{\mathrm{p}}^{\mathrm{climax}}$, r_{ao} and Ekman pumping; both rate estimates are lower in regions of Ekman downwelling and elevated in regions of Ekman up-

welling (Figs. 4, S14). This correspondence in part might result from the mean Ekman upwelling directly bringing nutrients into the euphotic layers, but this is likely a small contribution due to upwelling rates being extremely slow (Tagliabue et al., 2014). The more dominant way for Ekman forcing to modulate phytoplankton production is likely by setting the background stratification and nutricline properties, and allowing for nutrient transport along isopycnals (Naveira Garabato et al., 2017). In regions like the ACC, where deep isopycnals outcrop, the along-isopycnal nutrient transport can result from strong mesoscale and submesoscale stirring and would support blooms in regions of high EKE (Rosso et al., 2014, 2016; Balwada et al., 2018).

To the north of the ACC, Ekman downwelling likely results in a deep nutricline and nutrient limitation year round, leading to low values of $r_{\mathrm{p}}^{\mathrm{climax}}$ and r_{ao}. Elevated rates of production in the ACC, where isopycnals outcrop, might be suggestive of (sub)mesoscale nutrient supply at work. However, it is hard to exactly disentangle the eddy driven transport of deep water to the surface from from the localized aeolian and benthic sources of iron in the ACC. It is possible that the two mechanisms interact, with the benthic sources releasing nutrients into deep waters near topography, which are then brought to the surface via strong along isopycnal eddy stirring (Ardyna et al., 2019). Johnson et al. (2017) showed that the annual net community production (ANCP) was highest in the ACC region where the mixed layers were the deepest. One might expect light limitation driven by deep mixing to produce the lowest ANCP rates in this region, but it is appears that the dissolved iron supplied by high rates of mixing and stirring act to reduce the chronic iron limitation in the open Southern Ocean (Fig. 5). The very high rates to the south of the Polar Front are likely associated with the iron fertilization via sea ice melt (Boyd & Ellwood, 2010; Boyd et al., 2012; McGillicuddy et al., 2015; Ardyna et al., 2019).

4.3 Zonally Averaged Atlantic, Indian & Pacific Sector Climatologies

The previous sections discussed different bloom phases observed by individual floats and the statistics of their timings. In this section we provide an Eulerian view by averaging the bulk phytoplankton biomass and growth rates in three zonal sectors: the Atlantic (70E-20W), Indian (20W-180W), and Pacific (180E-70E) sectors of the Southern Ocean. The choice to average zonally, while maintaining a distinction between the three sectors, is motivated by the sparse spatial coverage of the data set, satellite based chlorophyll measurements showing lower chlorophyll concentrations in the Pacific sector rel-

ative to the other sectors (Thomalla et al., 2011; Ardyna et al., 2017), and the quasi-zonal nature of ACC fronts in different sectors. Climatological Hovmöller diagrams (Fig. 5) in latitude vs time were generated by averaging over all the data points in a zonal sector after weighting the data points with a Gaussian kernel of width 1.6° in latitude and 0.43 months (Locally Weighted Scatterplot Smoothing; LOWESS). As $\langle C_p \rangle$ followed a log-normal distribution, we applied the Gaussian kernel to $\ln \langle C_p \rangle$ and then took the exponent of the filtered data.

The climatology of bulk vertically integrated biomass $\langle C_p \rangle$ shows a clear seasonal cycle, with one major bloom per year, and the timing of apex shifts later in the year further south (Fig. 5**a**,**d**). Higher values of $\langle C_p \rangle (> 2$ g C $m^{-2})$ are mostly confined in the months when surface heat flux ($\mathcal{H}$) is positive during the austral summer (zero crossing of mean flux is shown as red lines). Due to shorter summers, indicated by PAR (black contours), blooms are constrained to fewer months in the south while the northern blooms are more diffused, consistent with the spread in bloom phase timings shown in Fig. 3. The Indian and Atlantic sectors have overall more biomass than the Pacific, likely due to more aeolian and lithogenic iron sources (Boyd & Ellwood, 2010; Swart et al., 2015).

In conjunction with biomass, the accumulation rates (r_p) are also evaluated in the same manner (Fig. 5**b**,**e**,**h**). The zonally averaged accumulation starts ($r_p > 0$) substantially before the timing of the mixed layer depth maxima (not shown) or when heat flux switches sign. At the time scales under consideration, the lag between change in heat flux and mixed layer restratification is not discernible (Taylor & Ferrari, 2010, 2011). Phytoplankton accumulation starting during the mixed layer deepening phase is in consensus with the timing plots in the previous section, where onset happens before the deepest mixed layers are observed. This observation is in agreement with the dilution-recoupling hypothesis of Behrenfeld (2010), which suggests that a deepening mixed layer reduces the phytoplankton and zooplankton concentrations and thus grazing pressure. These reduced grazing rates result in bulk phytoplankton increase, while the concentration of phytoplankton might be very low and even decreasing. The peak accumulation rates are often observed closer to the time when the heat flux changes sign, particularly around 50-60S, indicating a possible acceleration in growth rates as the mixed layers start to shoal (similar to those observed in the North Atlantic; Mignot et al., 2018).

Figure 5**c**,**f**,**i** show the climatological zonal mean of Ekman pumping and surface eddy kinetic energy (EKE) in each sector plotted against latitude. Consistent with the strength of the blooms (Fig. 4), the seasonal amplitude of $\langle C_p \rangle$ is generally low at latitudes where Ekman pumping is negative ($w_E < 0$). Local maxima of $\langle C_p \rangle$ align with the zonal-mean EKE maxima associated with the ACC in each sector around 55S, with correspondence in the Pacific being the most prominent (Fig. 5). In the Indian sector around 64S, there is a secondary maximum aligning with a peak in Ekman upwelling ($w_E > 0$), which is also a region close to and under the SIZ. The maximum in EKE around 40S in the Atlantic and Indian sector comes from a combination of high EKE in Brazil Current down stream of the Drake Passage and the Agulhas Current (Fig. 4), and does not display a very significant peak in $\langle C_p \rangle$. There is a small peak in the Atlantic sector around 40S, but this might be fortuitous, as these latitude ranges do not have a lot of floats (Fig. 1**a**).

5 Discussion and Conclusions

The seasonal cycle of phytoplankton carbon biomass in the open Southern Ocean has been of long interest to the oceanographic and biogeochemical community, due to its relevance to the biological carbon pump. Satellite observations have greatly enhanced our understanding of this seasonal cycle, and the factors controling its dynamics (Field et al., 1998; J. Moore & Abbott, 2000; Arrigo et al., 2008; Venables & Moore, 2010; Thomalla et al., 2011; Sallée et al., 2015; Verdy & Mazloff, 2017; Ardyna et al., 2017). Satellites, however, only capture the surface signature of primary production, and can be limited by the presence of clouds and sea-ice, which are plentiful in the Southern Ocean. Here, we present the first in-situ estimates of the phytoplankton carbon biomass seasonality in the open Southern Ocean observed by the biogeochemical (BGC) Argo floats deployed by the SOCCOM and SOCLIM projects. While limited in spatial coverage relative to satellites, these autonomous platforms provide year-round profiles of optical backscatter in the top 2000 m, allowing us to provide an estimate independent of chlorophyll, which is known to vary depending on the species and physiological state of phytoplankton (Geider, 1987; Geider et al., 1998; Behrenfeld & Boss, 2003; Haëntjens et al., 2017; Erickson & Thompson, 2018), and to explore the three-dimensional structure of phytoplankton dynamics. We highlight the main results in the form of a schematic (Fig. 6).

The subtropical zone (STZ) is the region to the north of the ACC, where PAR is plentiful year round, mixed layers are relatively shallow, the circulation is slow, and strat-

ification is characteristic of subtropical ocean gyres. This region is characterized by a mean Ekman downwelling, which in conjunction with flat isopycnals results in deep nutriclines (McClain et al., 2004; Wilson & Coles, 2005). The summer to winter contrasts in heat fluxes and winds is not significantly large to produce deep winter mixed layers, which could otherwise tap signficantly into the nutricline. The phytoplankton are, thus, constantly nutrient limited, resulting in the small amplitude of the seasonal cycle. Episodic mixing, resulting from storms (Carranza & Gille, 2015), and isopycnal heaving (Song et al., 2016) can sustain some phytoplankton growth, but this does not result in a very large annual cycle (Thomalla et al., 2011). Phytoplankton often exist below the mixed layer in this region, suggesting that the mixed layer is shallower than the euphotic layer.

The Antarctic Circumpolar Current (ACC) region is characterized by strong mean and transient currents, outcropping isopycnals that provide a pathway between the deep ocean and the surface (Naveira Garabato et al., 2017), mean Ekman upwelling, and deep winter mixed layers (Holte et al., 2017). Phytoplankton in this region may be PAR limited, not due to insufficient insolation, but due to mixing causing the phytoplankton to spend time out of the euphotic layers. The phytoplankton biomass in this region is greater than in the other two regions, including in austral summer, and has a large seasonal amplitude, with accumulation ($r_{\mathrm{p}} > 0$) starting few months prior to the timing of the deepest mixed layers. The accumulation prior to mixed-layer shoaling is consistent with the hypothesis of reduced grazing pressure during deep mixed layers leading to accumulation (Behrenfeld, 2010). Previous studies have shown that iron limitation is relieved in the open Southern Ocean by the deep winter mixed layers tapping into the ferricline (Tagliabue et al., 2014; Llort et al., 2015), and it is likely that (sub)mesoscale eddy stirring also brings up tracers including nutrients along the sloping isopycnals (Gnanadesikan et al., 2015; Balwada et al., 2018; Freilich & Mahadevan, 2019). Productivity in the ACC is highly spatially variable and concentrated in several blooms located at or just downstream of major topographic features (Sokolov & Rintoul, 2007). This is likely due to nutrient delivery to the euphotic zone via multiple processes that can occur where flow-bathymetry interactions enhance eddy tranport (Rosso et al., 2014, 2016; Ardyna et al., 2019), and where currents impinge on topography including upwelling (Gille et al., 2014) and generation of Taylor columns (Meredith et al., 2003; Prend et al., submitted).

The seasonal sea ice zone (SIZ) is to the south of the Polar Front, which experiences light limitation partially due to polar nights and the presence of sea-ice. This re-

gion is associated the subpolar Ross and Weddell gyres and is characterized by mean Ekman upwelling. The ecosystem in this region experiences an explosive phytoplankton growth once the sea ice recedes during austral spring (Briggs et al., 2018), but the duration of the growth season is extremely limited. The melting sea-ice is also a potential source of iron to relieve the nutrient limitation (Boyd & Ellwood, 2010).

Our estimate of phytoplankton seasonality based on profiling flows permit us to make a critical assessment of other methods that rely primarily on observations of surface chlorophyll concentrations (J. Moore & Abbott, 2000; Arrigo et al., 2008; Thomalla et al., 2011; Ardyna et al., 2017). Some recent studies have tried to consider evolution of the bulk biomass, rather than just the surface signature, using ancillary mixed-layer depth estimates and an assumption of vertical homogeneity of phytoplankton concentration over the depth of the mixed layer (Behrenfeld, 2010; Sallée et al., 2015). However, this is no substitute for truly depth-dependent measurements. Our results suggest that in the Southern Ocean, such surface-derived estimates can result in underestimating the bulk biomass, and sometimes even fail to reproduce the temporal variability. We define the surface concentration (C_p^{surf}) as the average concentration in the top 50 dbar. This averaging depth is arbitrary, but changing this depth criterion did not influence the results qualitatively. A corresponding bulk biomass is then estimated by multiplying C_p^{surf} by the observed mixed-layer depth (h_{ML}), similar to the estimate used by Sallée et al. (2015). The dashed green lines in the bottom row of Fig. 2 show that this proxy for bulk biomass has limited success. The proxy bulk biomass captures the approximate seasonal pattern for the float to the south of the Polar Front (Fig. 2**d**), as both $\langle C_p \rangle$ and $C_p^{surf} \times h_{ML}$ peak in January. However, $C_p^{surf} \times h_{ML}$ is out of phase with $\langle C_p \rangle$ for the float in the gyre (Fig. 2**f**) where the mixed layers are shallow, and a significant amount of biomass is present below the mixed-layer base. The comparison for the float in the ACC is also less than satisfactory (Fig. 2**e**), with the proxy showing weaker amplitude and estimating the apex too soon. Comparing $\langle C_p \rangle$ and $C_p^{surf} \times h_{ML}$ over the whole time series of each float showed that the latter is smaller in amplitude than the former, and the difference is greater at northern latitudes (Figs. 2, S7-S9). We examined all SOCCOM and SOCLIM float profiles and found this relation ($\langle C_p \rangle > C_p^{surf} \times h_{ML}$) to hold in most cases (Fig. S10). While the comparison made here is not completely fair to satellite based studies, it does suggest that some caution is needed when interpreting them; regardless

of the depth of the mixed layer, satellite observations may miss subsurface vertical structures in biogeochemical variables (Carranza et al., 2018).

We have presented the basin-wide averaged annual phytoplankton cycle in the Southern Ocean from in-situ observations (Fig. 5), and have only scratched the surface of what can be learned from this growing data set. We hope that this work will spur the interest of the wider community to further explore and critique this data set, and perform dedicated investigations into some of the more speculative elements of this work. Regional scale investigations (e.g Ardyna et al., 2019; Prend et al., submitted) are needed to understand the details of the spatial variations in biology. Careful investigations are needed to understand the biases introduced in the observations of time series by the Argo float quasi-Lagrangian sampling and 10-day temporal resolution, and the potential for studying synoptic time-scale variability. Our results show that vertically integrated biomass can be high even if concentration itself is low. Depending on the timing of blooms, wintertime enhancement in submesoscale vertical velocities can subduct this organic matter to depth (Omand et al., 2015; Llort et al., 2018; Erickson & Thompson, 2018), and indicates the significance of quantifying the timing and biomass of blooms.

Acknowledgments

This research was supported by NASA Award NNX16AJ35G as part of the SWOT Science Team. Abernathey acknowledges additional support from NSF Award OCE-1553593. The code used for the analysis in this study is available on Github (`doi:10.5281/zenodo.3336575`). Gille acknowledges NSF awards PLR-1425989 and OCE-1658001. Data were collected and made freely available by the Southern Ocean Carbon and Climate Observations and Modeling (SOCCOM) Project funded by the National Science Foundation, Division of Polar Programs (NSF PLR -1425989), supplemented by NASA (NNX14AP49G), the Southern Ocean and Climate Field Studies with Innovative Tools (SOCLIM) Project funded by the Foundation BNP Paribas and the Massachusetts Water Resource Authority, and by the International Argo Program and the NOAA programs that contribute to it. (`http://www.argo.ucsd.edu`, `http://argo.jcommops.org`). The BGC-Argo data used for this study can be downloaded from `http://soccom.ucsd.edu/floats/SOCCOM_data_ref.html` for SOCCOM and `ftp://ftp.ifremer.fr/ifremer/argo` for SOCLIM. Computational resources for BSOSE were provided by NSF XSEDE resource grant OCE130007.

AVISO products were were processed by SSALTO/DUACS and distributed by AVISO+ (`https://www.aviso.altimetry.fr`) with support from CNES.

References

Ardyna, M., Claustre, H., Sallée, J.-B., D'Ovidio, F., Gentili, B., Van Dijken, G., ... Arrigo, K. R. (2017). Delineating environmental control of phytoplankton biomass and phenology in the southern ocean. *Geophysical Research Letters*, *44*(10), 5016–5024.

Ardyna, M., Lacour, L., Sergi, S., dOvidio, F., Salle, J.-B., Rembauville, M., ... Claustre, H. (2019). Hydrothermal vents trigger massive phytoplankton blooms in the southern ocean. *Nature Communications*, *10*, 2451.

Arrigo, K. R., van Dijken, G. L., & Bushinsky, S. (2008). Primary production in the southern ocean, 1997–2006. *Journal of Geophysical Research: Oceans*, *113*(C8).

Balwada, D., Smith, K. S., & Abernathey, R. (2018). Submesoscale vertical velocities enhance tracer subduction in an idealized antarctic circumpolar current. *Geophysical Research Letters*.

Behrenfeld, M. J. (2010). Abandoning sverdrup's critical depth hypothesis on phytoplankton blooms. *Ecology*, *91*(4), 977–989.

Behrenfeld, M. J., & Boss, E. (2003). The beam attenuation to chlorophyll ratio: an optical index of phytoplankton physiology in the surface ocean? *Deep Sea Research Part I: Oceanographic Research Papers*, *50*(12), 1537–1549.

Behrenfeld, M. J., Boss, E., Siegel, D. A., & Shea, D. M. (2005). Carbon-based ocean productivity and phytoplankton physiology from space. *Global biogeochemical cycles*, *19*(1).

Behrenfeld, M. J., & Boss, E. S. (2018). Student's tutorial on bloom hypotheses in the context of phytoplankton annual cycles. *Global change biology*, *24*(1), 55–77.

Boss, E., & Behrenfeld, M. (2010). In situ evaluation of the initiation of the north atlantic phytoplankton bloom. *Geophysical Research Letters*, *37*(18).

Boyd, P. W., Arrigo, K., Strzepek, R., & Dijken, G. (2012). Mapping phytoplankton iron utilization: Insights into southern ocean supply mechanisms. *Journal of Geophysical Research: Oceans*, *117*(C6).

592 Boyd, P. W., & Ellwood, M. J. (2010). The biogeochemical cycle of iron in the
593 ocean. *Nature Geoscience*, *3*(10), 675–682.

594 Briggs, E. M., Martz, T. R., Talley, L. D., Mazloff, M. R., & Johnson, K. S. (2018).
595 Physical and biological drivers of biogeochemical tracers within the seasonal
596 sea ice zone of the southern ocean from profiling floats. *Journal of Geophysical*
597 *Research: Oceans*, *123*(2), 746–758.

598 Bushinsky, S. M., Gray, A. R., Johnson, K. S., & Sarmiento, J. L. (2017). Oxygen in
599 the southern ocean from argo floats: Determination of processes driving air-sea
600 fluxes. *Journal of Geophysical Research: Oceans*, *122*(11), 8661–8682.

601 Carranza, M. M., & Gille, S. T. (2015). Southern ocean wind-driven entrainment en-
602 hances satellite chlorophyll-a through the summer. *Journal of Geophysical Re-*
603 *search: Oceans*, *120*(1), 304–323.

604 Carranza, M. M., Gille, S. T., Franks, P. J., Johnson, K. S., Pinkel, R., & Girton,
605 J. B. (2018). When mixed layers are not mixed. storm-driven mixing and
606 bio-optical vertical gradients in mixed layers of the southern ocean. *Journal of*
607 *Geophysical Research: Oceans*, *123*(10), 7264–7289.

608 Carval, T., Keeley, R., Takatsuki, Y., Yoshida, T., Schmid, C., Goldsmith, R., ...
609 others (2014). *Argo users manual v3. 2.* Argo Data Management, 119pp,
610 http://www. argodatamgt. org.

611 de Boyer Montégut, C., Madec, G., Fischer, A. S., Lazar, A., & Iudicone, D. (2004).
612 Mixed layer depth over the global ocean: An examination of profile data
613 and a profile-based climatology. *Journal of Geophysical Research: Oceans*,
614 *109*(C12).

615 Deppeler, S. L., & Davidson, A. T. (2017). Southern ocean phytoplankton in a
616 changing climate. *Frontiers in Marine Science*, *4*.

617 Dutkiewicz, S., Follows, M. J., & Parekh, P. (2005). Interactions of the iron and
618 phosphorus cycles: A three-dimensional model study. *Global Biogeochemical*
619 *Cycles*, *19*(1).

620 Erickson, Z. K., & Thompson, A. (2018). The seasonality of physically-driven ex-
621 port at submesoscales in the northeast atlantic ocean. *Global Biogeochemical*
622 *Cycles*.

623 Field, C. B., Behrenfeld, M. J., Randerson, J. T., & Falkowski, P. (1998). Primary
624 production of the biosphere: integrating terrestrial and oceanic components.

science, *281*(5374), 237–240.

Forward, R. B. (1976). Light and diurnal vertical migration: photobehavior and photophysiology of plankton. In *Photochemical and photobiological reviews* (pp. 157–209). Springer.

Fox-Kemper, B., Ferrari, R., & Hallberg, R. (2008). Parameterization of mixed layer eddies. part i: Theory and diagnosis. *Journal of Physical Oceanography*, *38*(6), 1145–1165.

Freilich, M. A., & Mahadevan, A. (2019). Decomposition of vertical velocity for nutrient transport in the upper ocean. *Journal of Physical Oceanography*(2019).

Geider, R. J. (1987). Light and temperature dependence of the carbon to chlorophyll a ratio in microalgae and cyanobacteria: implications for physiology and growth of phytoplankton. *New Phytologist*, *106*(1), 1–34.

Geider, R. J., Maclntyre, H. L., & Kana, T. M. (1998). A dynamic regulatory model of phytoplanktonic acclimation to light, nutrients, and temperature. *Limnology and oceanography*, *43*(4), 679–694.

Gent, P. R., Willebrand, J., McDougall, T. J., & McWilliams, J. C. (1995). Parameterizing eddy-induced tracer transports in ocean circulation models. *Journal of Physical Oceanography*, *25*(4), 463–474.

Gille, S. T., Carranza, M. M., Cambra, R., & Morrow, R. (2014). Wind-induced upwelling in the kerguelen plateau region. *Biogeosciences*, *11*, 6389-6400.

Gnanadesikan, A., Pradal, M.-A., & Abernathey, R. (2015). Isopycnal mixing by mesoscale eddies significantly impacts oceanic anthropogenic carbon uptake. *Geophysical Research Letters*, *42*(11), 4249–4255.

Graff, J. R., Westberry, T. K., Milligan, A. J., Brown, M. B., Dall'Olmo, G., van Dongen-Vogels, V., ... Behrenfeld, M. J. (2015). Analytical phytoplankton carbon measurements spanning diverse ecosystems. *Deep Sea Research Part I: Oceanographic Research Papers*, *102*, 16–25.

Gray, A. R., Johnson, K. S., Bushinsky, S. M., Riser, S. C., Russell, J. L., Talley, L. D., ... Sarmiento, J. L. (2018). Autonomous biogeochemical floats detect significant carbon dioxide outgassing in the high-latitude southern ocean. *Geophysical Research Letters*, *45*(17), 9049–9057.

Gruber, N., Landschützer, P., & Lovenduski, N. S. (2019). The variable southern ocean carbon sink. *Annual review of marine science*, *11*, 159–186.

Haëntjens, N., Boss, E., & Talley, L. D. (2017). Revisiting ocean color algorithms for chlorophyll a and particulate organic carbon in the southern ocean using biogeochemical floats. *Journal of Geophysical Research: Oceans*, *122*(8), 6583–6593.

Holte, J., Talley, L. D., Gilson, J., & Roemmich, D. (2017). An argo mixed layer climatology and database. *Geophysical Research Letters*, *44*(11), 5618–5626.

Johnson, K. S., Plant, J. N., Coletti, L. J., Jannasch, H. W., Sakamoto, C. M., Riser, S. C., ... others (2017). Biogeochemical sensor performance in the soccom profiling float array. *Journal of Geophysical Research: Oceans*, *122*(8), 6416–6436.

Lévy, M., Bopp, L., Karleskind, P., Resplandy, L., Éthé, C., & Pinsard, F. (2013). Physical pathways for carbon transfers between the surface mixed layer and the ocean interior. *Global Biogeochemical Cycles*, *27*(4), 1001–1012.

Leymarie, E., Penkerc'h, C., Vellucci, V., Lerebourg, C., Antoine, D., Boss, E., ... Claustre, H. (2018). Proval: A new autonomous profiling float for high quality radiometric measurements. *Frontiers in Marine Science*, *5*, 437.

Llort, J., Langlais, C., Matear, R., Moreau, S., Lenton, A., & Strutton, P. G. (2018). Evaluating southern ocean carbon eddy-pump from biogeochemical-argo floats. *Journal of Geophysical Research: Oceans*, *123*(2), 971–984.

Llort, J., Lévy, M., Sallée, J.-B., & Tagliabue, A. (2015). Onset, intensification, and decline of phytoplankton blooms in the southern ocean. *ICES Journal of Marine Science: Journal du Conseil*, *72*(6), 1971–1984.

Marshall, J., & Speer, K. (2012). Closure of the meridional overturning circulation through southern ocean upwelling. *Nature Geoscience*, *5*(3), 171.

Mazloff, M., Cornuelle, B., Gille, S., & Verdy, A. (2018). Correlation lengths for estimating the large-scale carbon and heat content of the southern ocean. *Journal of Geophysical Research: Oceans*, *123*(2), 883–901.

McClain, C. R., Signorini, S. R., & Christian, J. R. (2004). Subtropical gyre variability observed by ocean-color satellites. *Deep Sea Research Part II: Topical Studies in Oceanography*, *51*(1-3), 281–301.

McDougall, T. J., & Barker, P. M. (2011). Getting started with teos-10 and the gibbs seawater (gsw) oceanographic toolbox. *SCOR/IAPSO WG*, *127*, 1–28.

McGillicuddy, D. J., Sedwick, P. N., Dinniman, M. S., Arrigo, K. R., Bibby, T. S.,

Greenan, B. J., ... others (2015). Iron supply and demand in an antarctic shelf ecosystem. *Geophysical Research Letters*, *42*(19), 8088–8097.

McKinley, G. A., Fay, A. R., Lovenduski, N. S., & Pilcher, D. J. (2017). Natural variability and anthropogenic trends in the ocean carbon sink. *Annual Review of Marine Science*, *9*(1), 125–150.

Meredith, M. P., Watkins, J. L., Murphy, E. J., Cunningham, N. J., Wood, A. G., Korb, R., ... Vivier, F. (2003). An anticyclonic circulation above the northwest georgia rise, southern ocean. *Geophysical Research Letters*, *30*(20).

Mignot, A., Ferrari, R., & Claustre, H. (2018). Floats with bio-optical sensors reveal what processes trigger the north atlantic bloom. *Nature Communications*, *9*(1).

Mignot, A., Ferrari, R., & Mork, K. A. (2016). Spring bloom onset in the nordic seas. *Biogeosciences*, *13*(11), 3485–3502.

Moore, C., Mills, M., Arrigo, K., Berman-Frank, I., Bopp, L., Boyd, P., ... others (2013). Processes and patterns of oceanic nutrient limitation. *Nature geoscience*, *6*(9), 701.

Moore, J., & Abbott, M. (2000). Phytoplankton chlorophyll distributions and primary production in the southern ocean. *Journal of Geophysical Research: Oceans*, *105*(C12), 28709–28722.

Moore, J., Lindsay, K., Doney, S., Long, M., & Misumi, K. (2013). Marine ecosystem dynamics and biogeochemical cycling in the community earth system model [cesm1 (bgc)]: Comparison of the 1990s with the 2090s under the rcp4. 5 and rcp8. 5 scenarios. *Journal of Climate*, *26*(23), 9291–9312.

Morel, A., Huot, Y., Gentili, B., Werdell, P. J., Hooker, S. B., & Franz, B. A. (2007). Examining the consistency of products derived from various ocean color sensors in open ocean (case 1) waters in the perspective of a multi-sensor approach. *Remote Sensing of Environment*, *111*(1), 69–88.

Naveira Garabato, A. C., MacGilchrist, G. A., Brown, P. J., Evans, D. G., Meijers, A. J., & Zika, J. D. (2017). High-latitude ocean ventilation and its role in earth's climate transitions. *Philosophical Transactions of the Royal Society A: Mathematical, Physical and Engineering Sciences*, *375*(2102), 20160324.

Omand, M. M., D'Asaro, E. A., Lee, C. M., Perry, M. J., Briggs, N., Cetinić, I., & Mahadevan, A. (2015). Eddy-driven subduction exports particulate organic

carbon from the spring bloom. *Science*, *348*(6231), 222–225.

Osman, M. B., Das, S. B., Trusel, L. D., Evans, M. J., Fischer, H., Grieman, M. M., ... Saltzman, E. S. (2019). Industrial-era decline in subarctic atlantic productivity. *Nature*, 1.

Parekh, P., Follows, M. J., & Boyle, E. (2004). Modeling the global ocean iron cycle. *Global Biogeochemical Cycles*, *18*(1).

Prend, C. J., Gille, S. T., Talley, L. D., Mitchell, B. G., Rosso, I., & Mazloff, M. R. (submitted). Physical drivers of phytoplankton bloom initiation in the southern ocean's scotia sea. *Journal of Geophysical Research: Oceans*.

Redi, M. H. (1982). Oceanic isopycnal mixing by coordinate rotation. *Journal of Physical Oceanography*, *12*(10), 1154–1158.

Riser, S. C., Swift, D., & Drucker, R. (2018). Profiling floats in soccom: Technical capabilities for studying the southern ocean. *Journal of Geophysical Research: Oceans*.

Roesler, C., Uitz, J., Claustre, H., Boss, E., Xing, X., Organelli, E., ... others (2017). Recommendations for obtaining unbiased chlorophyll estimates from in situ chlorophyll fluorometers: A global analysis of wet labs eco sensors. *Limnology and Oceanography: Methods*, *15*(6), 572–585.

Rosso, I., Hogg, A. M., Matear, R., & Strutton, P. G. (2016). Quantifying the influence of sub-mesoscale dynamics on the supply of iron to southern ocean phytoplankton blooms. *Deep Sea Research Part I: Oceanographic Research Papers*, *115*, 199–209.

Rosso, I., Hogg, A. M., Strutton, P. G., Kiss, A. E., Matear, R., Klocker, A., & van Sebille, E. (2014). Vertical transport in the ocean due to sub-mesoscale structures: Impacts in the kerguelen region. *Ocean Modelling*, *80*, 10–23.

Sallée, J.-B., Llort, J., Tagliabue, A., & Lévy, M. (2015). Characterization of distinct bloom phenology regimes in the southern ocean. *ICES Journal of Marine Science: Journal du Conseil*, *72*(6), 1985–1998.

Sarmiento, J. L. (2013). *Ocean biogeochemical dynamics*. Princeton University Press.

Schlitzer, R. (2002). Carbon export fluxes in the southern ocean: results from inverse modeling and comparison with satellite-based estimates. *Deep Sea Research Part II: Topical Studies in Oceanography*, *49*(9-10), 1623–1644.

Siegel, D. A., Buesseler, K. O., Doney, S. C., Sailley, S. F., Behrenfeld, M. J., & Boyd, P. W. (2014). Global assessment of ocean carbon export by combining satellite observations and food-web models. *Global Biogeochemical Cycles*, *28*(3), 181–196.

Siegenthaler, U., & Sarmiento, J. (1993). Atmospheric carbon dioxide and the ocean. *Nature*, *365*(6442), 119.

Silsbe, G. M., Behrenfeld, M. J., Halsey, K. H., Milligan, A. J., & Westberry, T. K. (2016). The cafe model: A net production model for global ocean phytoplankton. *Global Biogeochemical Cycles*, *30*(12), 1756–1777.

Sokolov, S., & Rintoul, S. R. (2007). On the relationship between fronts of the antarctic circumpolar current and surface chlorophyll concentrations in the southern ocean. *Journal of Geophysical Research: Oceans*, *112*(C7).

Song, H., Marshall, J., Munro, D. R., Dutkiewicz, S., Sweeney, C., McGillicuddy, D. J., & Hausmann, U. (2016). Mesoscale modulation of air-sea co2 flux in drake passage. *Journal of Geophysical Research: Oceans*, *121*(9), 6635–6649.

Stukel, M. R., & Ducklow, H. W. (2017). Stirring up the biological pump: Vertical mixing and carbon export in the southern ocean. *Global Biogeochemical Cycles*.

Swart, S., Thomalla, S. J., & Monteiro, P. (2015). The seasonal cycle of mixed layer dynamics and phytoplankton biomass in the sub-antarctic zone: A high-resolution glider experiment. *Journal of Marine Systems*, *147*, 103–115.

Tagliabue, A., Sallée, J.-B., Bowie, A. R., Lévy, M., Swart, S., & Boyd, P. W. (2014). Surface-water iron supplies in the southern ocean sustained by deep winter mixing. *Nature Geoscience*, *7*(4), 314–320.

Taylor, J. R., & Ferrari, R. (2010). Buoyancy and wind-driven convection at mixed layer density fronts. *Journal of Physical Oceanography*, *40*(6), 1222–1242.

Taylor, J. R., & Ferrari, R. (2011). Shutdown of turbulent convection as a new criterion for the onset of spring phytoplankton blooms. *Limnology and Oceanography*, *56*(6), 2293–2307.

Thomalla, S. J., Fauchereau, N., Swart, S., & Monteiro, P. M. S. (2011). Regional scale characteristics of the seasonal cycle of chlorophyll in the southern ocean. *Biogeosciences*, *8*(10), 2849–2866.

Venables, H., & Moore, C. M. (2010). Phytoplankton and light limitation in the

790 southern ocean: Learning from high-nutrient, high-chlorophyll areas. *Journal*
791 *of Geophysical Research: Oceans*, *115*(C2).
792 Verdy, A., & Mazloff, M. (2017). A data assimilating model for estimating south-
793 ern ocean biogeochemistry. *Journal of Geophysical Research: Oceans*, *122*(9),
794 6968–6988.
795 Westberry, T., Behrenfeld, M., Siegel, D., & Boss, E. (2008). Carbon-based primary
796 productivity modeling with vertically resolved photoacclimation. *Global Bio-*
797 *geochemical Cycles*, *22*(2).
798 Wilkin, J. L., & Morrow, R. A. (1994). Eddy kinetic energy and momentum flux in
799 the southern ocean: Comparison of a global eddy-resolving model with altime-
800 ter, drifter, and current-meter data. *Journal of Geophysical Research: Oceans*,
801 *99*(C4), 7903–7916.
802 Williams, R. G., & Follows, M. J. (2011). *Ocean dynamics and the carbon cycle:*
803 *Principles and mechanisms*. Cambridge University Press.
804 Wilson, C., & Coles, V. J. (2005). Global climatological relationships between satel-
805 lite biological and physical observations and upper ocean properties. *Journal of*
806 *Geophysical Research: Oceans*, *110*(C10).

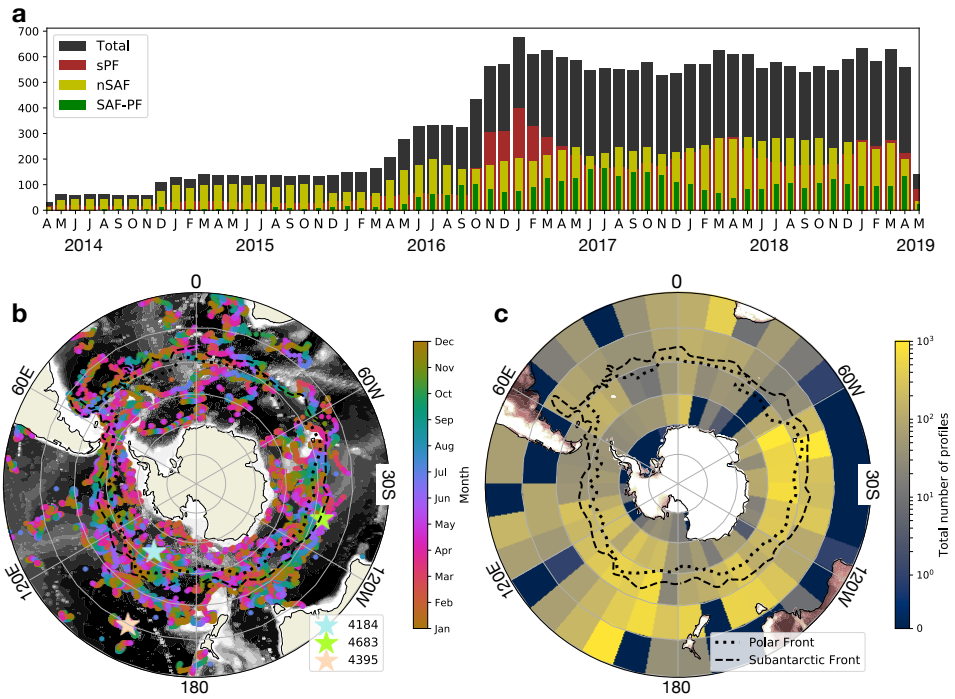

Figure 1. Data availability of the entire SOCCOM and SOCLIM data set. **a** Time series of the number of $\langle C_p \rangle$ data points at any given month of the year with north of the Subantarctic Front (SAF) in yellow, between SAF and the Polar Front (PF) in green, and south of PF in brown. The SOCLIM float data started from October 2016, resulting in a large increase in total data availability. **b** The geographical location and month of all datapoints of vertically integrated C_p and the climatological position of the fronts were taken from orsi1995meridional. The black shading shows the bathymetry. The mean position of three representative floats (ID: 5904134, 5904395, 5904683) are shown as the stars. **c** The cumulative number of profiles over the whole data set aggregated over 10° lat-lon boxes.

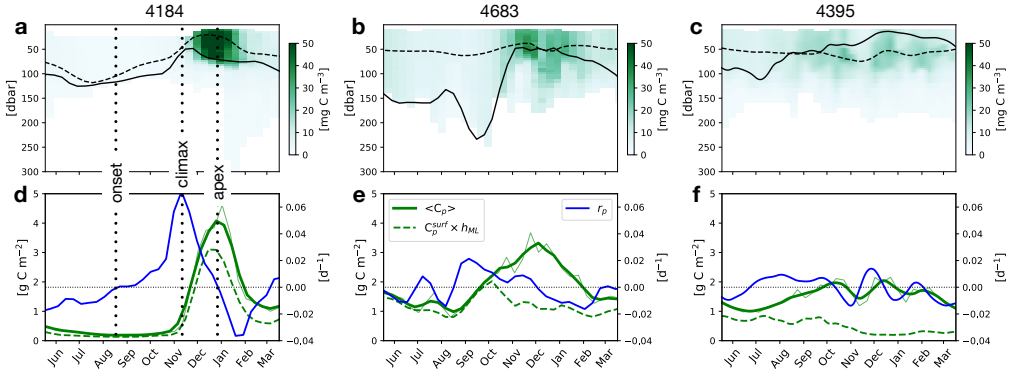

Figure 2. Time series of de-spiked and interpolated C_p masked out based on the Chl cut off (**a-c**) plotted against pressure for the floats shown in Fig. 1**b**. The full time series of each float is given in the Supporting Information. The black solid (dashed) lines show h_{ML} (h_{PAR}). **d-f** Time series of the vertically integrated carbon $\langle C_p \rangle$, surface carbon concentration multiplied by h_{ML} and accumulation rates after a 30-day running mean is applied. The thin green lines show $\langle C_p \rangle$ before the running mean.

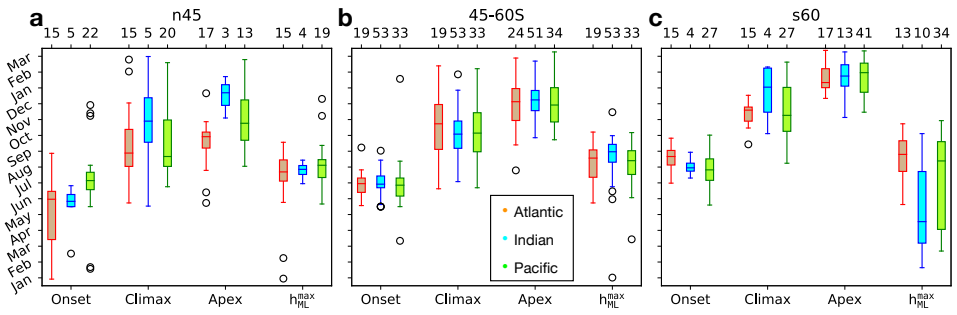

Figure 3. Box plot of the month each spring bloom phase (onset, climax and apex) and mixed-layer depth maxima takes place for the latitudinal band north of 45S (n45) **a**, 45-60S **b** and south of 60S (s60) **c**. Atlantic, Indian, and Pacific sectors are shown in orange, blue and green respectively. The solid line within the box shows the median, boxes the interquartile range, and whiskers the 95 percentile. The top x axes show the number of data that go into generating the box plots.

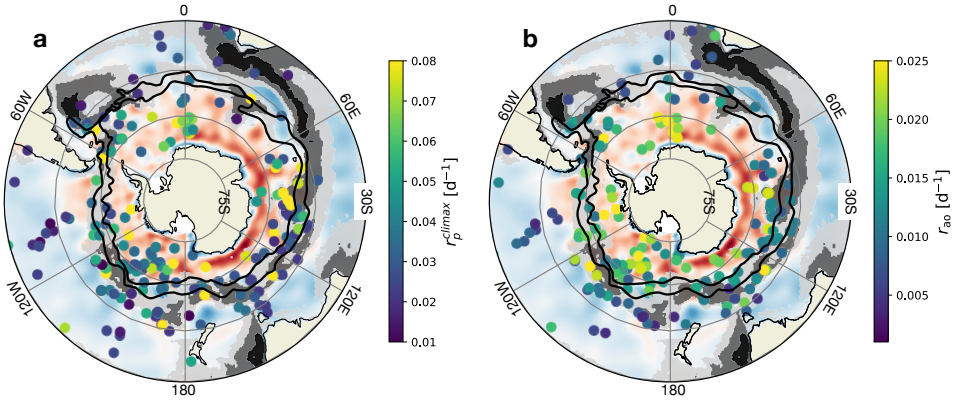

Figure 4. **a** Accumulation rate at the climax of each bloom ($r_{\mathrm{p}}^{\mathrm{climax}}$), and rate of vertically integrated biomass increase from onset to apex of each bloom (r_{ao}) **b** plotted against geographical location. Red shadings show the annual mean of Ekman pumping, while blue indicates Ekman suction, using the wind-stress curl from BSOSE after a Gaussian spatial filter with 3° radius was applied, and black contours show the climatology of surface EKE in [m^2 s^{-2}] over the years of 1997-2017. Values below 0.009 m^2 s^{-2} are masked out.

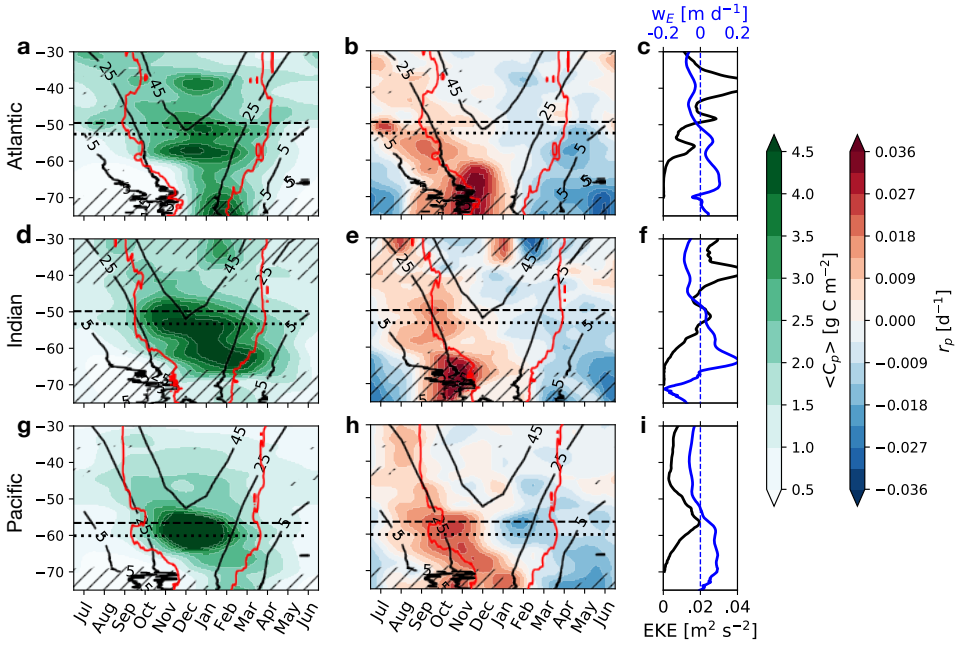

Figure 5. Hovmöller diagrams of the monthly climatological zonally-averaged $\langle C_p \rangle$ and r_p plotted against latitude in the Indo-Atlantic sector (70W-180E; **a**,**b**), and Pacific sector (180E-290E; **d**,**e**) for the five years of float data available. The black hashes indicate grids with less than 10 profiles and the black dashed (dotted) line shows the zonal mean of the climatological position of SAF (PF). The black contours show the zonal-mean monthly climatology of PAR (5, 25, 45 [Ein m^{-2} d^{-1}]) observed from the SeaWiFS satellite, and the time at which the sign of temperature flux changes taken from the BSOSE is shown in red contours. **c**,**f** The zonal mean of climatological surface EKE (black) and Ekman pumping derived from wind stress in SOSE (blue) for each sector.

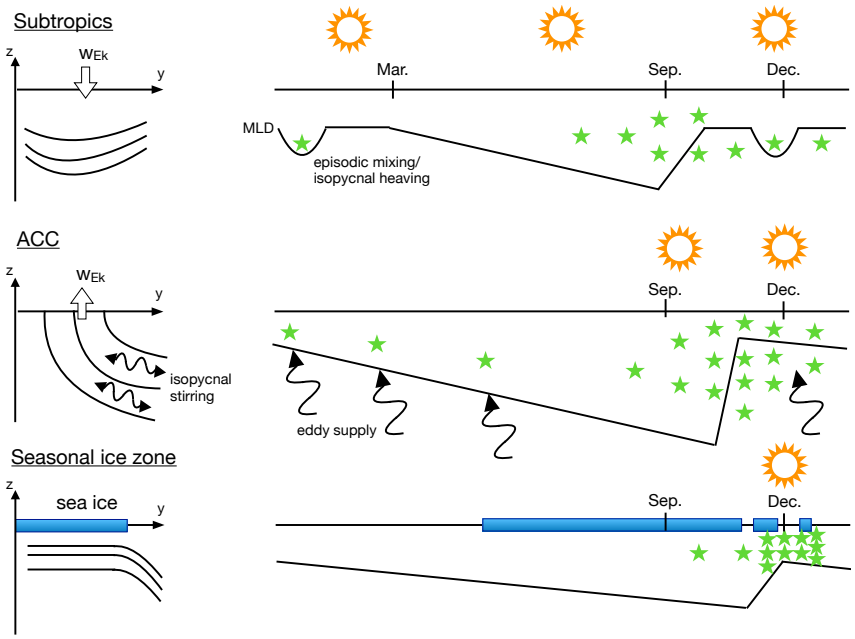

Figure 6. Schematic of the different bloom regimes in the Subtropical Zone (STZ), Antarctic Circumpolar Current (ACC) and Seasonal Ice Zone (SIZ). The black solid lines in the left column indicate the isopycnals. The right column shows the seasonal cycle of the mixed-layer depth (MLD, black line), phytoplankton (green stars, with number of stars indicating concentration), significant levels of PAR (symbol of the sun) for each zone. The squiggly black arrows indicate eddy-driven transport processes along isopycnal.